

Asymmetric Spacer in Dion–Jacobson Halide Perovskites Induces Staggered Alignment to Direct Out-of-Plane Carrier Transport and Enhances Ambient Stability Simultaneously

Shuang Yu, Mohamed Abdellah, Tõnu Pullerits, Kaibo Zheng,* and Ziqi Liang*

Dion–Jacobson (DJ)-type 2D halide perovskites present superior environmental stability and a narrower bandgap, yet a contradiction between charge transport and stability remains to be resolved. Herein, it is shown that both symmetry and substitution of the organic spacer in DJ perovskites synergistically direct the narrow interlayer spacing, staggered spacer alignment, and regular phase arrangement, thereby promoting out-of-plane carrier transport and ambient stability. Compared to its symmetric *para*-xylylenediamine (PDMA) counterpart, the asymmetric 2-(4-aminophenyl)ethylamine (PMEA) spacer largely aids in compressing the inorganic octahedra layer to form a non-confinement structure with decreased exciton binding energy, while stacked benzene rings enable a staggered alignment of spacers. Such non-confined structures are less remarkable in *meta*-substituted diamine-based DJ perovskites than those *para*-ones, which retard carrier transport from 2D to quasi-2D phases. The preferential PMEA spacer however requires a long relaxation time to form a dense and ordered staggered alignment, which is realized by a slight addition of strong-coordinating DMSO into the DMF solvent, thus decelerating crystallization and further optimizing lamellar orientation. As a result, a best efficiency of $\approx 12\%$ is achieved in (PMEA)MA₃Pb₄I₁₃ based p-i-n type planar solar cells. Importantly, such unencapsulated devices can maintain 81% initial efficiencies after storage in ambient conditions ($\approx 60\%$ relative humidity, $\approx 20^\circ\text{C}$) for 700 h.


1. Introduction

Two-dimensional (2D) metal halide perovskites (MHPs) have recently emerged in the burgeoning development of various perovskite materials due to their excellent ambient stability.

S. Yu, Z. Liang
Department of Materials Science
Fudan University
Shanghai 200433, China
E-mail: zqliang@fudan.edu.cn

M. Abdellah, T. Pullerits, K. Zheng
Department of Chemical Physics and NanoLund
Lund University
Box 124, Lund 22100, Sweden
E-mail: kzheng@kemi.dtu.dk

K. Zheng
Department of Chemistry
Technical University of Denmark
Kongens Lyngby DK-2800, Denmark

 The ORCID identification number(s) for the author(s) of this article can be found under <https://doi.org/10.1002/adfm.202104342>.

DOI: 10.1002/adfm.202104342

2D MHPs mainly adopt two general formulas—Ruddlesden–Popper (RP)-type $L_2A_{n-1}B_nX_{3n+1}$ and Dion–Jacobson (DJ)-type $LA_{n-1}B_nX_{3n+1}$, where L is the organic spacer, A is a monovalent organic cation, B is a divalent metal cation, X is a halide anion, and n represents the number of inorganic layers.^[1] To compare RP and DJ 2D perovskites, the primary difference is the alignment of the corresponding inorganic $[BX_6]^{4-}$ slabs, that is, (1/2, 1/2, displacement) in RP phases and (0, 0, displacement) in DJ phases.^[2] Compared to the relatively weak van der Waals (VDW) bonding among monovalent organic cations (i.e., $R-NH_3^+$) in RP-phased perovskites, $^+H_3N-R-NH_3^+$ diamine molecules in DJ-type perovskites circumvent such VDW gaps by forming strong hydrogen interactions between one spacer and two adjacent inorganic layers, which leads to efficient carrier transport. Moreover, the stiffer interlayer packing in DJ perovskites caused by a single spacer layer allows for less distortion of the inorganic framework, which could be characterized by linear equatorial Pb–I–Pb angles, than in RP analogues with dual spacer layers, thus rendering better alignment and less displacement of octahedral $[BX_6]^{4-}$.^[3,4]

Inspired by the classical RP-type butylamine (BA) spacer, a series of DJ-type aliphatic straight-chain spacers was first proposed.^[5–13] In 2014, for instance, the Karunadasa group first reported a DJ-type monolayer 2D perovskite based on spacer–2,2'-(ethylenedioxy)bis(ethylammonium) (EDBE), which obtained a stable 9% PLQE under continuous irradiation.^[5] Such aliphatic straight-chain spacer based 2D perovskites entail longer carbon chains to improve moisture resistance, which however inhibit charge transport between octahedral interlayers. Numerous spacers bearing aliphatic branched chains as well as aliphatic- and aromatic-rings have been thus incorporated to decrease the interlayer spacing, strengthen the interstacking of organic spacers and weaken the octahedral distortion of the inorganic layers.^[15–23] **Figure 1a** summarizes the above structural evolution of the cation spacer, which exhibits a sequentially decreasing interlayer spacing from chain-like to ring-like molecules when having the same number of carbon atoms. The smaller ring-like spacers tend to have narrow interlayer spacing compared to the chain-like analogues.^[24] However, these ring-like spacers suffer from large steric hindrance,

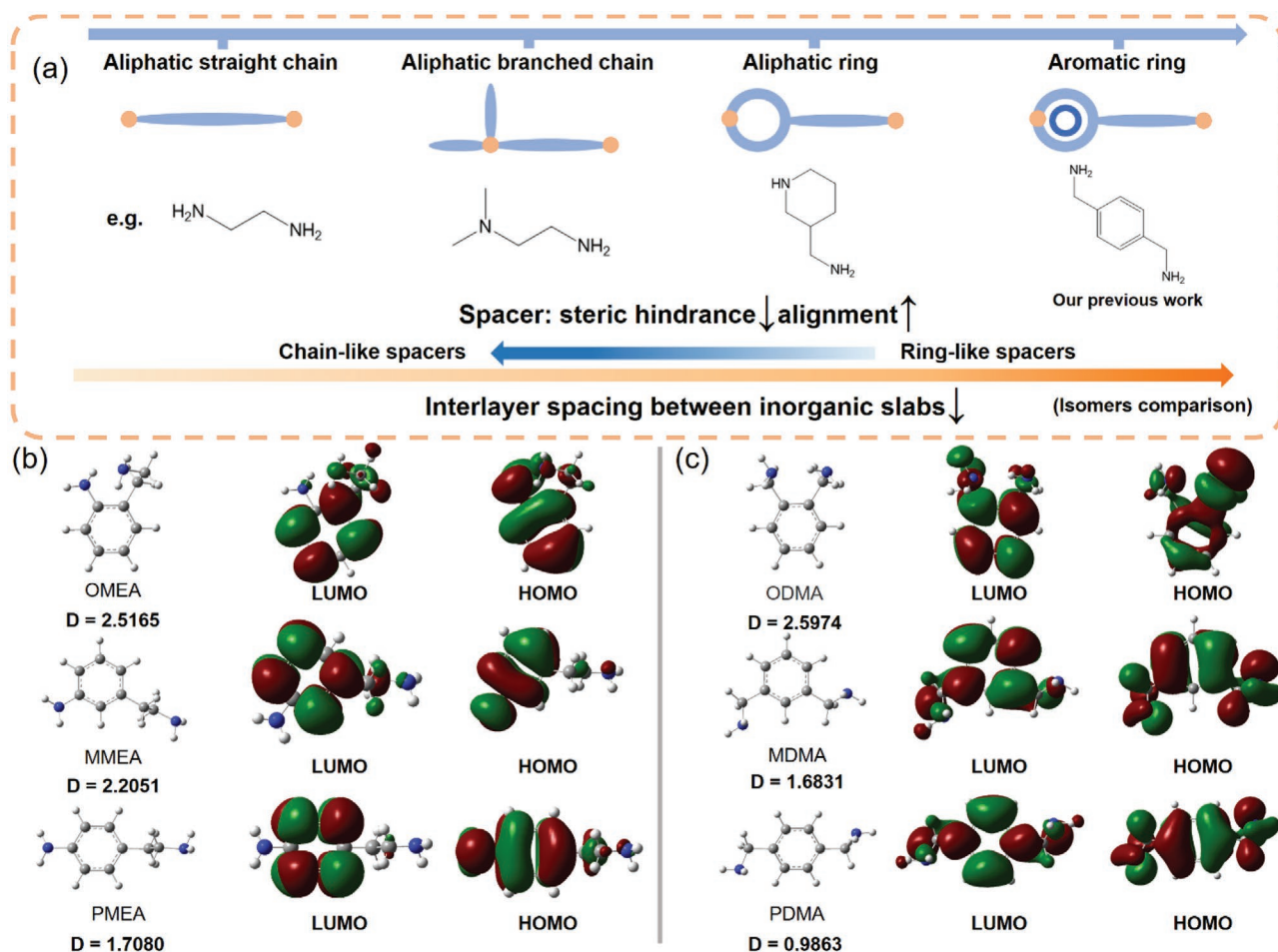


Figure 1. a) Comparison of various aromatic diammonium cations employed in 2D DJ perovskites in literature. Electron-density distribution of 2D DJ-type spacers with realistic main conformation bearing b) asymmetric aromatic cations with amino-groups located at *ortho*-, *meta*- and *para*-positions (abbreviated as OMEA, MMEA, and PMEAs) in the LUMO and HOMO energy levels as well as dipole moments (D) in comparison to those having c) symmetric aromatic cation analogues (ODMA, MDMA, and PDMA). Blue, gray, and white balls represent nitrogen, carbon, and hydrogen atoms, respectively.

which could distort the configuration of inorganic layers (e.g., Pb–I–Pb angles) and elongate the spacer rearrangement (that is, the longer relaxation time) during the transformation from the oriented 3D-like phase to the 2D phase, potentially leading to unfavorable issues such as random orientation, poor crystallinity, irregular phase distribution, and thermodynamic instability.^[25,26] Such steric hindrance can be suppressed in aromatic-ring versus aliphatic-ring spacers caused by increased co-planarity, thereby leading to smaller interlayer spacings.^[6] Moreover, π -conjugated aromatic-ring spacers display the increased electron cloud density, which further promotes interlayer charge transport.^[27–36] These spacers, however, demand a longer relaxation time to form stable 2D perovskites with an aligned spacer arrangement, presumably due to a large hindrance of stacking arrangement between the neighboring benzene rings in the same horizontal direction. Therefore, there is an urgent need for such a spacer design criterion that directs us to shorten the interlayer spacing of 2D perovskites while satisfying the dense and orderly arrangement of spacer molecules. In a preliminary study, Kanatzidis and colleagues studied

heterocyclic spacers and their substitution patterns, which provided an effective method for screening new organic spacers via molecular design.^[14]

2. Results and Discussion

Our previous work found the non-confinement structure in *p*-phenylenediamine (PDMA) spacer-based 2D DJ perovskite ($n > 3$) greatly promotes interlayer carrier transport.^[36] The non-confinement phases were rationalized in our previous study by i) a low exciton binding energy (E_b) that facilitates exciton dissociation, ii) a shortened interlayer spacing that overlaps the electron cloud between neighboring halide atoms, and iii) 3D bulk-like optical characteristics.^[36] Motivated by the beneficial effects of symmetric spacers, herein we attempt to further unravel how both symmetry and substitution of organic spacers in DJ perovskites impact the crystallization, phase composition, charge carrier dynamics, and device performance. We have therefore systematically investigated organic spacer cations

(denoted as L) of o , m , p -positioned phenylenediamine (i.e., ODMA, MDMA, PDMA) as symmetric spacers by taking one axis in the benzene ring plane as a rotation axis, and the corresponding o , m , p -(2-aminoethyl)aniline (i.e., OMEA, MMEA, PMEA) as asymmetric spacers, all of which are intercalated into the $[BX_6]^{4-}$ inorganic octahedra to produce 2D DJ-type $LMa_3Pb_4I_{13}$ ($n = 4$). A structural comparison of these symmetric and asymmetric spacers is shown in Figure 1b,c.

First, we employed density functional theory (DFT) to calculate the dipole moments as displayed in Figure 1b,c. We obtained the conformation with the lowest energy in the realistic case as the object of DFT calculation by comparing different substituent rotation angles via Gaussian simulation. The calculation shows that as the distance between two alkyl chains on the benzene ring increases gradually from the o -, m - to p -position, the dipole moment decreases accordingly. Such a trend is observed in both asymmetric and symmetric aromatic cations, although the change in the former is less pronounced than the latter, indicating that the electronic environment of the asymmetric structure is more stable.

We then turned to focus on m - and p -positioned spacers—PDMA, PMEA, MDMA, and MMEA—to unravel the impacts of their molecular symmetry on the crystalline structures and optical properties of 2D DJ perovskites while neglecting those structurally unstable o -positioned spacers. Generally, there is a strong tendency in 2D layered perovskite thin films to produce a mixture of multiple n -value phases when $n > 1$.^[37–39] Thus, in order to exclude the effect of the number of octahedral layers (i.e., n value) on organic spacer layers, we prepared neat 2D DJ perovskites with one inorganic octahedral layer (i.e., $n = 1$), denoted as MDMA-1, MMEA-1, PDMA-1 and PMEA-1. They show signature diffraction peaks ($2\theta < 10^\circ$) of low-dimensional halide perovskites at 8.39° , 7.69° , 7.10° , and 7.35° , which correspond to d -spacings of 10.53, 11.49, 12.44, and 12.02 Å, respectively, according to the Bragg's equation (Figure 2a). It can be further seen that only $para$ -substituted PDMA-1 and PMEA-1 display two intense perovskite peaks at 14.43° and 14.67° , respectively, which are however absent in m -substituted spacers. Accordingly, the sizes of one-layer octahedra are determined to be 6.18 Å (PDMA-1) and 6.08 Å (PMEA-1), which give rise to the corresponding interlayer spacings of 6.52 and 5.96 Å between inorganic slabs, respectively. The reduction in interlayer spacing in PMEA-1 is strongly related to the shorter VDW length of the spacer, that is, 11.38 Å for PDMA and 11.09 Å for PMEA as calculated from Figure S1 in the Supporting Information. Next, if the influence of the octahedral size is not taken into account, the interlayer spacing correlates positively with the VDW length of the spacer molecule. Note that the difference of interlayer spacing values between PDMA-1 and PMEA-1 (≈ 0.56 Å) is much larger than the VDW length difference (≈ 0.29 Å) between PDMA and PMEA, which results most likely from the more pronounced spacer compression in PMEA-1 compared to PDMA-1. In addition, as their benzene ring is not positioned at the center of the spacer molecule, the asymmetric spacers are prone to align in a staggered fashion, that is, an interdigitated arrangement, when schematically compared with symmetric analogues in Figure 2a. As a result, the thickened hydrophobic layer of these stacked benzene rings in the asymmetric PMEA spacer will protect the inorganic layers

more effectively from moisture diffusion. In short, a combination of small spacings and tightly staggered benzene rings in asymmetric $para$ -positioned spacer leads to noticeably high crystallinity that promotes interlayer charge transport along the perpendicular octahedral direction.

In contrast, the significantly reduced crystallinity of $meta$ -positioned spacers (MDMA-1 and MMEA-1) is found, which is ascribed to the adjacent substituents that prevent the spacer molecules from forming dense and aligned inorganic octahedral layers, as explained below. As shown in Figure S1, Supporting Information, the VDW widths of $meta$ -spacers (that is, 7.30 Å for MDMA, 7.27 Å for MMEA) are larger than $para$ -ones (that is, 7.00 Å for PDMA, 6.97 Å for PMEA). The adjacent octahedra spacing is determined to be ≈ 6 Å from the characteristic perovskite peak at $\approx 14^\circ$ in XRD patterns, which is smaller than the above VDW widths. Thus, the larger the VDW width of the molecule interposed between two inorganic octahedra, the more squeezed the spacing, resulting in a greater steric hindrance during the spacer arrangement. The increased steric hindrance further induces diverse hydrogen bonding patterns, which affect the Pb–I–Pb angle and E_g .^[26] Therefore, we speculate that the $meta$ -spacers may take a longer time to arrange regularly with the uniform orientation between inorganic octahedral layers compared to $para$ -spacers, leading to poor crystallinity in both MDMA-1 and MMEA-1. As such, the degree of crystallinity at $n = 4$ can be ranked as PDMA-4 > MMEA-4 > PMEA-4 > MDMA-4, which can be derived from the half-peak width of one 14° perovskite characteristic peak as shown in Figure 2b and also listed in Table S1, Supporting Information, suggesting the larger the half-height width, the lower the crystallinity. In addition, all these four samples show diffraction peaks at $\approx 8^\circ$ as also observed in our previous study because of the nonconfinement effect in high- n (e.g., $n = 4$) DJ perovskites compressed by squeezing of inorganic octahedral layers.^[36]

We have previously revealed that DMSO is a strong coordinating solvent that slows down the crystallization process in PEA based 2D perovskites by forming intermediate complexes in the precursor solution.^[36] Such slow crystallization benefits the alignment of organic spacers during the conversion from orientated 3D-like phase to 2D perovskite, in particular for asymmetric spacer structures, which greatly aids in forming regularly arranged spacer layers of interspersed benzene-ring stacks. Upon DMSO treatment, as shown in Figure 2b, the crystallinity of MDMA-4 is increased while that of other samples declines. The crystallization influence of DMSO on all four samples is suggested by the noticeable disparity in intensity ratio of the diffraction peaks of the 14° and 28° crystal planes as shown in Table S2, Supporting Information. The DMSO treatment might induce a complex trade-off that occurs among the crystallization rate, nucleation energy, and spacer re-orientation among others, which leads to various effects on different samples. In addition, DMSO treatment effectively suppresses the formation of excessive PbI_2 as produced by imperfect crystallization in PDMA-4 samples.

Furthermore, we exploited the grazing-incidence wide-angle X-ray scattering (GIWAXS) technique to gain an insight into the above crystallographic orientation. By varying different incident angles, we probed the surface (0.05°) and bulk (0.2°) orientation of the thin film, respectively. The results are displayed in

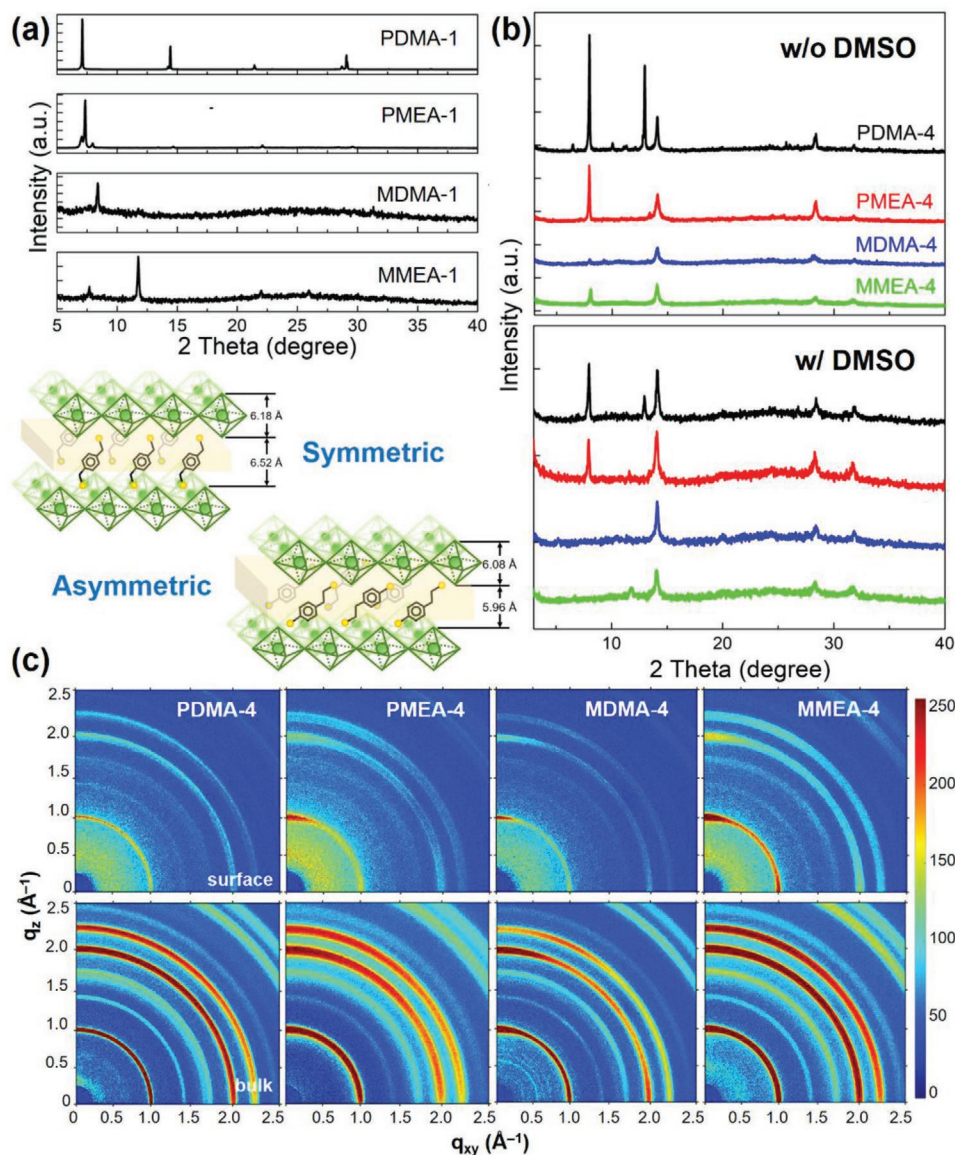


Figure 2. XRD patterns of symmetric (PDMA, MDMA) and asymmetric (PMEA, MMEA) cations based 2D DJ perovskites. a) Neat PDMA-1 and PME-1 based perovskites ($n = 1$) and their corresponding schematic sketches of molecular structures and calculated interlayer *d*-spacings. Comparing the crystallization response of structural effect on those 2D perovskites ($n = 4$): b) without (w/o) and with (w/) DMSO treatment. c) GIWAXS images of PDMA-4, PME-4, MDMA-4, and MMEA-4 on the surface and in bulk at an incidence angle of 0.05° and 0.2° , respectively.

Figure 2c and Figure S2, Supporting Information, summarizes the GIWAXS plots of all samples with a range of incidence angles before and after DMSO treatment. The samples all show a noticeable diffraction signal in the $q_z = 0$ direction at 1.0 \AA^{-1} , indicating that the quasi-2D phases on the surface tend to align preferentially parallel to the substrate. In the asymmetric samples, the signal of horizontal orientation on the surface is enhanced whereas the vertical orientation begins to show up.

The transient absorption measurement as shown later demonstrates that the quasi-2D phases are dominant for all the samples and hence the difference in confinement effect between cross- and in-plane orientations is negligible. In this regard, the effect of whether the directional or the random orientations is more decisive than which direction the molecules

get oriented in. Consequently, the preferential horizontal and vertical orientations in asymmetric PME-4 and MMEA-4 suggest a more regular phase arrangement (i.e., a more uniform lattice orientation) than those of the symmetric PDMA-4 and MDMA-4. Of particular note is symmetric PDMA-4 and asymmetric MMEA-4 samples feature ring-like structures, indicative of random orientation.

To investigate the effects of both asymmetric spacer and DMSO treatment on optical properties, we characterized the optical absorption and photoluminescence (PL) spectra in thin films, as shown in Figure 3a,b. The symmetric spacers of PDMA-4 and MDMA-4 exhibit multiple excitonic absorption peaks at 514, 562, and 607 nm, implying the presence of multiple *n* value phases. In contrast, the asymmetric spacers

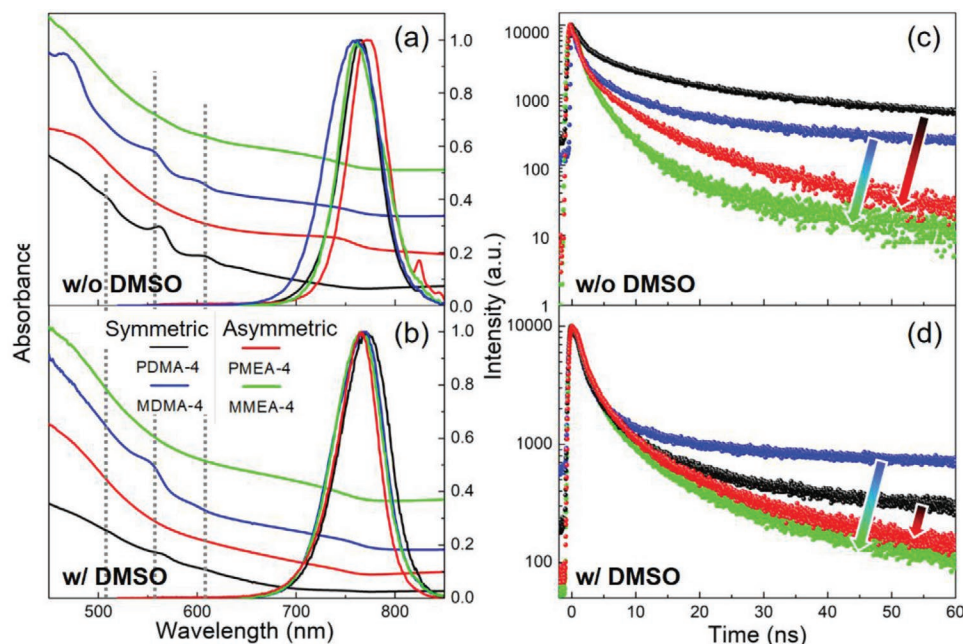


Figure 3. Optical spectra of symmetric and asymmetric 2D DJ perovskite ($n = 4$) thin films without and with DMSO treatment: (a,b) Steady-state absorption and PL spectra as well as (c,d) transient TRPL decays ($\lambda_{\text{ex}} = 505$ nm). Note that black line = PDMA-4, red line = PMEA-4, blue line = MDMA-4 and green line = MMEA-4.

of PMEA-4 and MMEA-4 show optical absorption characteristics of 3D perovskite (Figure 3a). After DMSO treatment, the original small n -value excitonic peaks of symmetric 2D perovskite are weakened, indicative of a decreased contribution from low-dimensional perovskite phases (Figure 3b). The steady-state PL spectra also reveal the subtle regulation of the asymmetric spacers on the phase structures of 2D DJ perovskites, which mainly assists to increase 3D phases as evidenced by the slight red-shifts of PL peaks, compared to symmetric analogues (Figure 3a). These 3D phases are attributed to the large π -conjugations with interlaced benzene-rings stacking under a shorter interlayer spacing, which affords a smaller E_g than the low-dimensional phases and thus can facilitate exciton splitting and carrier transport. After DMSO treatment, the PL peaks of different samples are found to be positioned at similar wavelengths, further indicating the gradual transformation of the neat 2D phase to a 3D-like phase (Figure 3b). In addition, the PL lifetimes are determined after biexponential fitting of time-resolved photoluminescence (TRPL) spectra in Figure 3c,d and then summarized in Table S3, Supporting Information, in which symmetric spacer based 2D perovskites exhibit longer lifetime than asymmetric ones, while the *para*-sites are longer than the *meta*-sites.

We further unveiled the effects on film morphology and stability, and the results are presented in Figure 4a,h,i, respectively. The surface of the neat symmetric PDMA-4 thin film exhibits stacked rod-shape crystals, which is consistent with our previous study,^[36] whereas asymmetric PMEA-4 shows an inhomogeneous distribution of small-sized grains filled around grain boundaries, suggesting that heterogeneity in crystalline growth is induced with the aid of an asymmetric spacer. Such a phenomenon is also evident in *meta*-spacers (i.e., MDMA and

MMEA) based 2D perovskite films. In MDMA-4, a uniform distribution of dense small-sized grains appears on the flat film surface, while in MMEA-4, some of the small grains grow into large ones accompanied by bigger pinhole-like defects. We therefore hypothesize that the orderly arrangement of MMEA spacers requires a longer relaxation time, which is difficult to attain under common experimental conditions. The pinhole defects in MMEA-4 due to imperfect crystallization are passivated by slowing down the crystallization caused by DMSO treatment, which is also evidenced by an increase in shunt resistance as shown in Figure S3, Supporting Information. Interestingly, as shown in the insets, the water contact angles of asymmetric spacer structures are larger than those of symmetric analogues in both the *para*- and *meta*-structures, indicating that asymmetric 2D perovskites are more stable against water. To confirm it, we further tested thin film stability when exposed to air under relative humidity (RH) of $60 \pm 5\%$ at 20 ± 2 °C. It is found that symmetric MDMA-4 and PDMA-4 show a yellow phase of decomposed PbI_2 at 168 and 672 h, respectively, while the asymmetric MMEA-4 and PMEA-4 remain stable as darkish films—characteristic of 2D perovskite phases—for over 1000 h. The extended air stability of 2D DJ perovskites is attributed to their markedly improved structural and optoelectronic properties such as enhanced carrier lifetime and mobility along with reduced defect density.

To sum up the above structural and morphological results, we constructed a model of asymmetric 2D DJ perovskites as schematically shown in Figure 4j that comprises the spontaneous generation of both non-confined 3D-like phases due to an extrusion of octahedral layers and confined 2D phases distributed at the grain boundaries of those 3D phases. The former act as major light absorbers while the latter effectively passivate

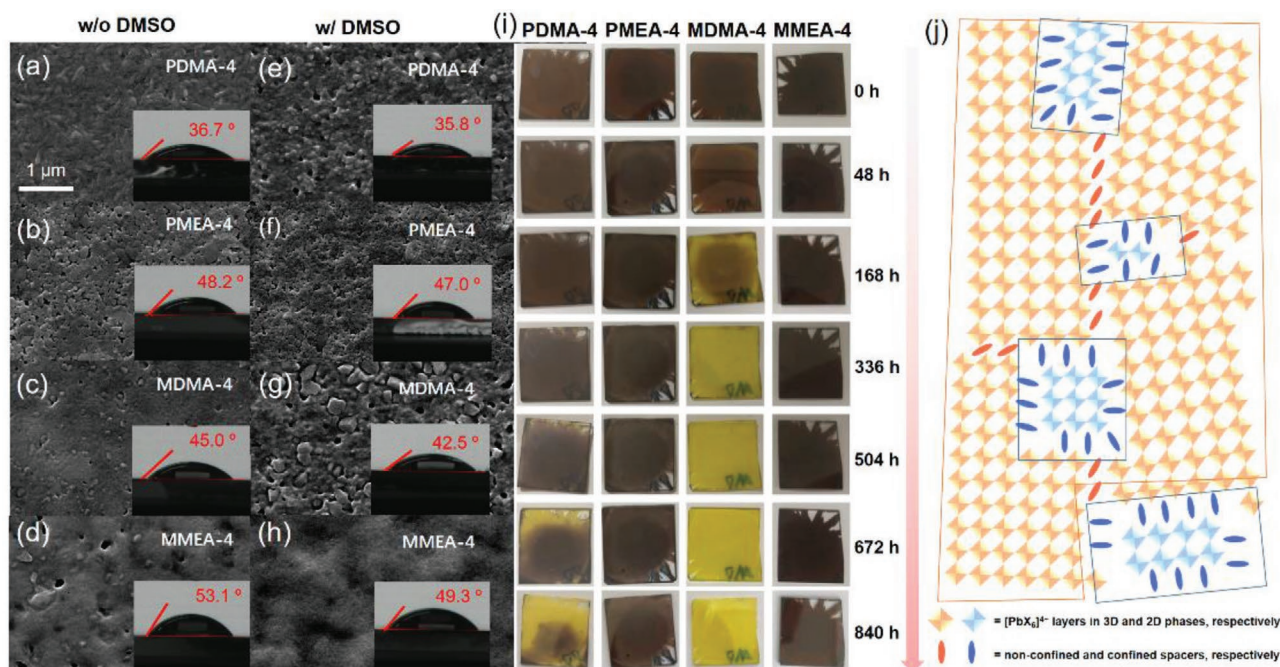


Figure 4. SEM topography images of symmetric and asymmetric 2D DJ perovskite thin films (a–d) without and (e–h) with DMSO treatment on glass substrate. Insets are the measured water contact angles. (i) Photographs of PDMA-4, PME-4, MDMA-4 and MMEA-4 thin films when exposed to a RH of $60 \pm 5\%$ at $20 \pm 2^\circ\text{C}$ for various lengths of time. (j) Schematic illustration of phase distribution in asymmetrical 2D perovskite thin film. Blue wireframe: 2D phase, Orange wireframe: nonconfinement phase and 3D phase.

morphological defects and suppress nonradiative recombination, yet their small sizes and discontinuous distribution make 2D perovskites difficult to form into long-range ordered crystal structures.

Then we employed transient absorption (TA) spectroscopy to reveal the photo-generated charge carrier dynamics of the above four 2D DJ perovskite thin films. **Figure 5a** shows the TA spectrogram of all 2D perovskite samples after 400 nm pump photo-excitation with the corresponding singular value decomposition (SVD) fitting attached at the lower panel. The TA spectra are mainly composed of the ground-state bleach (GB) bands of 2D (500–700 nm) and quasi-2D (700–750 nm) phases.^[40] The SVD fitting reveals four similar decay-associated spectral components for all four samples. The fastest components (530–900 fs, black curve) exhibit the negative GB of 2D phases in parallel with the positive signal at the position of quasi-2D phased GB. They manifest an excited-state depopulation in 2D phases concurrent with a population in quasi-3D phases, which is a fingerprint of photo-induced charge transfer in-between as depicted in the inset of the SVD results.^[37] The second component (red curve, 29–76 ps) features a broad negative band covering the wavelength range of both 2D and quasi-2D phases. Such simultaneous excited-state depopulation in two phases characterizes the interfacial charge recombination as illustrated in the inset diagram. The last two components (i.e., blue curve, 238–307 ps; green curve, >10 ns) with the same single GB band represent two pathways of excited state depopulation in the quasi-2D phase. According to our previous study, the suppressed quantum confinement in such quasi-2D phases facilitates the dissociation of Wannier excitons into free carriers.^[34] Therefore, we can assign the

former component with a hundred of ps lifetime to be the trap-mediated mono-molecular recombination of charge carriers, which is identical to the process in 3D perovskite. The last long-lived component shares a similar lifetime to those of PL decays in **Figure 3c**, and therefore should be attributed to the radiative carrier recombination. It is well-accepted that at $n > 4$ in 2D perovskites, the quasi-2D regime is approached where the quantum confinement and the thickness-dependent E_g are no longer pronounced. In this respect, changing n -value will only modify E_g to a slight extent. The broadening of the absorption band edge in MDMA-4 and PDMA-4 means the n -value varies within a wide range. Furthermore, we studied the effect of DMSO treatment on the charge carrier dynamics for the favorite PME-4 sample, as also shown in **Figure 5a**. It is found that the DMSO treatment does not change the proportion of low- n phases and 3D-like phases in samples and the inter-phase charge transfer, but can slightly increase the excited-state lifetime of the quasi-2D phases as indicated by the TA kinetics of the GB minimum.

Despite the similar lifetimes in each process among four samples, we find the GBs of the 2D phase observed in two symmetric (PDMA and MDMA) perovskites are drastically diminished in two asymmetric (PME-4 and MMEA) perovskites. This indicates the more dominant contribution of the quasi-2D phases in asymmetric 2D perovskites, which is in good agreement with the structural characterization results discussed above. Such a conclusion can be further verified by the reduced E_b in PME-4 as measured to be 121.8 meV relative to PDMA-4 (135.7 meV) by calculation from the fitting of integrated PL intensity in temperature-dependent PL measurements (**Figure 5b,c**). In fact, the generation of free carriers

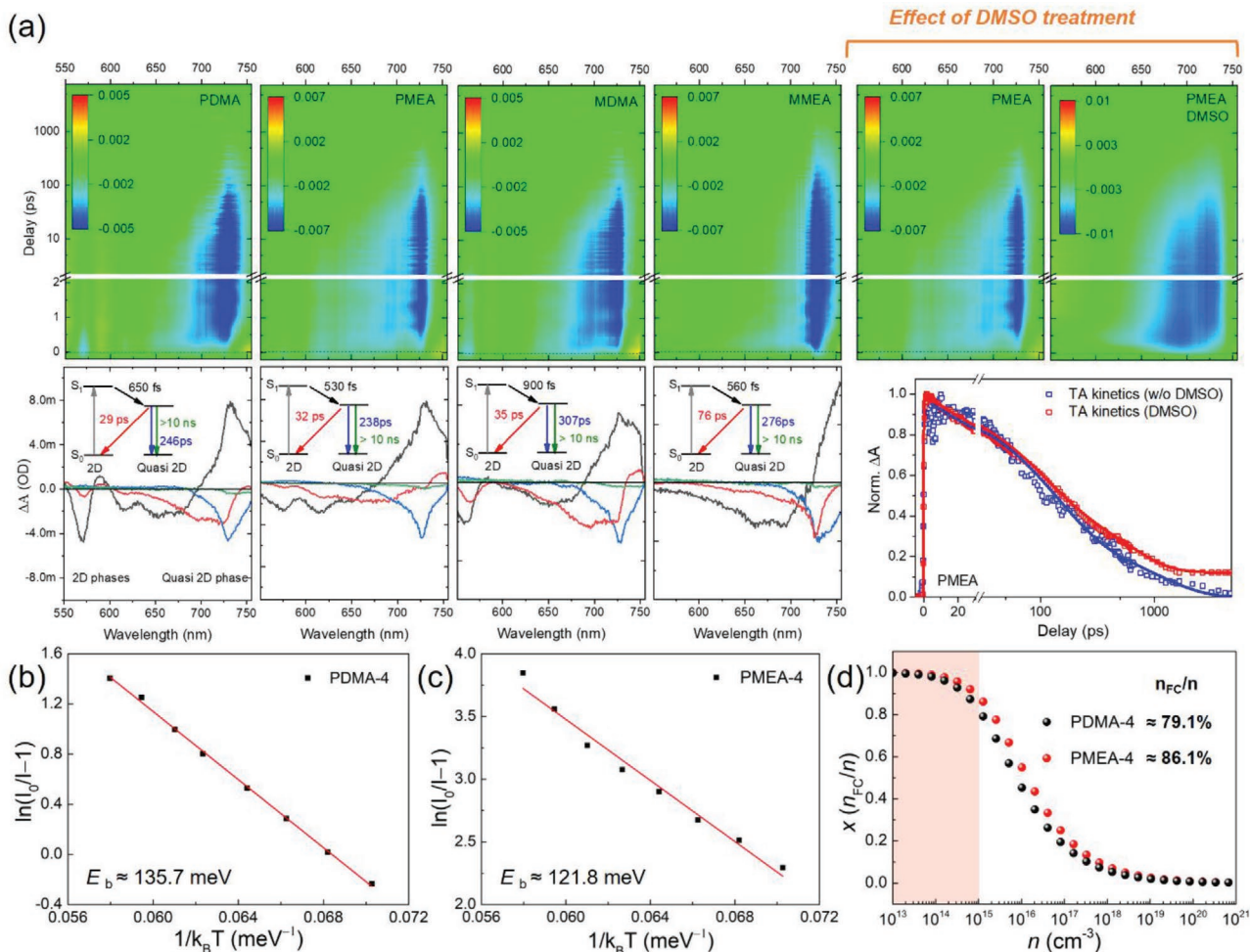


Figure 5. a) TA spectrograms and the corresponding SVD fitting results of symmetric and asymmetric 2D perovskite. Insets showing schematics of charge transfer between 2D and 3D phases and recombination pathways as analyzed from TA studies. Exciton binding energy measurement of b) symmetric and c) asymmetric 2D DJ perovskite ($n = 4$) and d) a simulation of the free charge fraction over the total excitation density ($x = n_{FC}/n$) at thermal equilibrium according to the Saha Langmuir equation.

and excitons in semiconductors should be a thermodynamic equilibrium that complies with the following Saha-Langmuir expression^[41]

$$\frac{x^2}{1-x} = \frac{1}{n} \left(\frac{2\pi m k_B T}{h^2} \right)^{1.5} e^{-\frac{E_b}{k_B T}} \quad (1)$$

where x is the ratio of free charges over the total density of excitation, n is the sum of free charge carriers (n_{FC}) and excitons (n_{exc}) giving the excitation density, m is the reduced mass of the exciton ($\approx 0.15 m_e$), E_b is the exciton binding energy, h is Planck's constant, and T is the temperature. The lower E_b of PMEAs than that of PDMA renders more efficient exciton dissociation in the dominant quasi-2D phase in PMEAs, as shown in Figure 5d. In addition, the narrower GB of the quasi-2D phase in two *para*-structured (PDMA, PMEAs) perovskites compared with their other two *meta*-structured counterparts further confirms the narrower n -value distribution and crystallinity acquired from the structural characterization.

Finally, we fabricated planar p-i-n type PSCs with a device configuration of ITO/PEDOT:PSS/(PDMA/PMEAs) $MA_3Pb_4I_{13}$ /PCBM/BCP/Ag. Figure 6a shows the photocurrent density-voltage ($J-V$) curves of the PDMA and PMEAs based 2D DJ perovskite devices that were measured at a scan rate of 100 mV s⁻¹ under AM 1.5G illumination and the detailed photovoltaic parameters and the forward and reverse scan curves are shown in Table S4 and Figure S4 in Supporting Information, respectively. The paradigm asymmetric PMEAs-based device without DMSO treatment achieves a respectable power conversion efficiency (PCE) of 9.27% with a high J_{SC} of 19.20 mA cm⁻², V_{OC} of 0.92 V and an FF of 53%, much higher than that of its symmetric PDMA-4 counterpart (4.91%). Upon DMSO treatment, the best efficiency is further largely boosted up to $\approx 12\%$ and the photovoltaic performance of various PMEAs-4 devices is summarized in Table S5, Supporting Information, among which the average efficiencies under reverse and forward scans reach 10.78 and 10.51%, respectively, with a negligible hysteresis factor of 0.025. The improved device performance originates mainly from the acquired remarkably higher J_{SC} of 23.44 mA cm⁻²

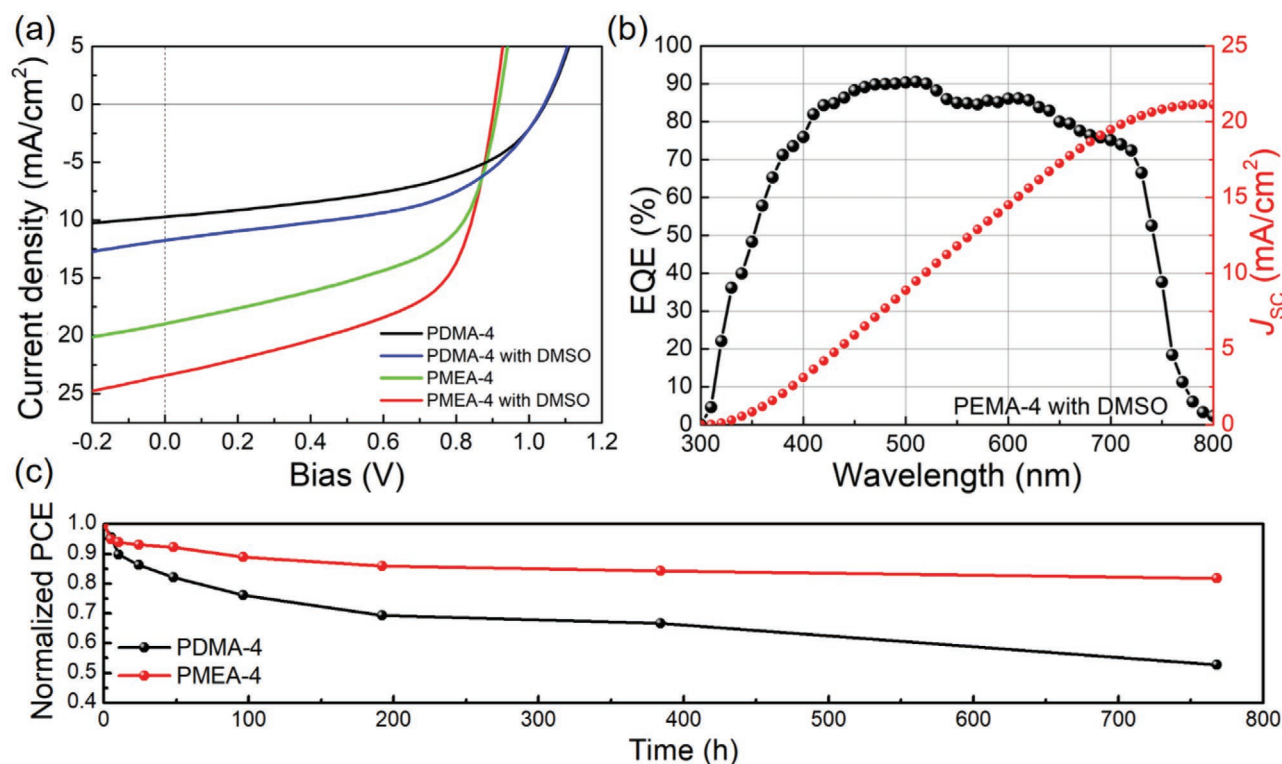


Figure 6. a) Photo- J - V curves of the optimal DJ perovskite solar cells based on ITO/PEDOT:PSS/(PMEA/PDMA)MA₃Pb₄I₁₃/PCBM/BCP/Ag under AM 1.5G simulated light irradiation and b) EQE profile of DMSO-treated the best-performing PMEA-4 based device. c) Normalized PCE of PDMA-4 cells with DMSO treatment as a function of exposure time under ambient conditions with RH of $60 \pm 5\%$ at $20 \pm 2^\circ\text{C}$.

due to the optimized crystallization and improved vertical crystal orientation as well as the presence of narrower- E_g non-confinement phases. As shown in Figure 6b, the external quantum efficiency (EQE) spectrum of the champion PMEA-4 device shows an onset of around 780 nm, which coincides with its absorbance spectrum (Figure 3b), and an integrated J_{SC} of 21.14 mA cm^{-2} , which is comparatively reduced due to the interference of oriented 2D perovskite with the polarization of the excitation light. The evolution of normalized PCEs for DMSO-treated PDMA-4 and PMEA-4 devices in an air atmosphere with a RH of $60 \pm 5\%$ at $20 \pm 2^\circ\text{C}$ is summarized in Figure 6c. The PMEA-4 device shows much better ambient stability by retaining $\approx 82\%$ of its initial PCE after 768 h (that is, 32 days) than the PDMA-4 device with a reduction to $\approx 53\%$ under the same conditions. As a final note, one latest study by Xu et al. mixed RP and DJ spacers in precursor solution and hence improved both charge transport and moisture stability, which represents a strategy complementary to this work.^[42]

3. Conclusion

To conclude, we have systematically investigated the influences of symmetry and substitution in aromatic spacer-based DJ layered perovskites on interlayer spacing, spacer alignment, phase arrangement, out-of-plane carrier transport and ambient stability. It is revealed that the *para*-substituted asymmetric spacer promotes the formation of non-confinement

phases with narrow interlayer spacing, thereby facilitating out-of-plane carrier transport, and meanwhile, the enlarged interlayer π -conjugation via an alignment of tightly stacked benzene rings significantly enhances ambient stability. However, the *meta*-spacers with less ordered alignment retard carrier transport from 2D to quasi-2D phases. Therefore, by prolonging the relaxation time of molecular stacking upon DMSO solvent treatment, the optimal PMEA-4 device delivers the best PCE of $\approx 12\%$ while maintaining excellent ambient stability. In the end, a short summary is explicitly presented in Figure S5, Supporting Information: 1) asymmetric spacers, relative to symmetric counterparts, help to enhance both phase orientation and stability; 2) *para*-positioned DJ perovskites (i.e., PDMA-4 and PMEA-4) yield narrower n -value distribution compared to *meta*-substituted perovskites (i.e., MDMA-4 and MMEA-4).

4. Experimental Section

Materials: PbI₂ and CH₃NH₃I were purchased from Maituowei Ltd. (China). Phenethylamine was purchased from Energy Chemical. All other chemicals were purchased from J&K Scientific, Ltd. (China). All the reagents were used as received.

Fabrication of 2D Perovskite Thin Films: The (PDMA/PMEA/MDMA/MMEA)MA₃Pb₄I₁₃ precursor solutions (40 wt%) prepared by mixing PbI₂, HI, CH₃NH₃I and PDMA at corresponding stoichiometric ratios in mixed solvent of DMF and DMSO (100:3 vol%). All the 2D perovskites films were obtained by spin-coating the precursor solutions at 5000 rpm for

60 s at room temperature. Toluene was dripped on the spinning wet 2D perovskite for 5 s. Part of the samples were treated by thermal annealing at 100 °C for 10 min.

Characterization: Optical absorption spectra of samples were acquired on an Agilent 8453 UV-Visible spectrophotometer. Steady-state photoluminescence was measured using a FluoroMax4 spectrofluorometer (HORIBA JOBIN YVON, Inc., Edison, NJ) with the excitation beam at 500 nm. The PL intensity was then corrected by absorbed photon numbers at the exciting light wavelength. X-ray diffraction pattern data for 2θ values were collected with a Bruker AX D8 Advance diffractometer with nickel filtered Cu $K\alpha$ radiation ($\lambda = 1.5406 \text{ \AA}$). Field-emission scanning electron microscopy images coupled with energy-dispersive X-ray elemental analysis were acquired on the Philips XL-30 field-emission gun at an accelerating voltage of up to 30 kV. Transient absorption (TA) experiments were performed by using a femtosecond pump-probe setup in a nitrogen atmosphere. Laser pulses (800 nm, 80 fs pulse length, 1 kHz repetition rate) were generated by a regenerative amplifier (Spitfire XP Pro) seeded by a femtosecond oscillator (Mai Tai SP, both Spectra Physics). The pump pulses at 400 nm were generated by a BBO crystal as a second harmonic of the laser. The used excitation photon fluxes are 3×10^{12} and 1.5×10^{14} photons cm^{-2} pulse $^{-1}$. For the probe, we used the super-continuum generation from a thin CaF_2 plate. The mutual polarization between the pump and probe beams was set to the magic angle (54.7°) by placing a Berek compensator in the pump beam. The probe pulse and the reference pulse were dispersed in a spectrograph and detected by a diode array (Pascher Instruments). In order to avoid photo-damage, the sample was moved to a fresh spot after each time delay point. The Global SVD analysis was performed with the Glotaran software package (<http://glotaran.org>). These methods yield more accurate fits of rate constants because they treat the full data set as a whole. A simple sequential decay model with various components is chosen for every fitting. Time-resolved photoluminescence (TRPL) spectra were obtained using a streak camera (Hamamatsu, C6860). The laser source is an amplified titanium/sapphire laser providing 800 nm 35 fs pulses at 2 kHz which is then frequency doubled for 400 nm excitation.

Device Fabrication and Measurements: ITO substrates were cleaned sequentially in an ultrasonic bath with deionized water, acetone, and isopropyl alcohol for 20 min, respectively, and then dried under nitrogen. The substrates were oxidized in UV-ozone for 20 min before use. The PEDOT:PSS layers were spin-coated on the patterned substrates at 3000 rpm for 60 s and annealed at 130 °C for 30 min. The substrates coated with PEDOT:PSS were transferred to an N_2 filled glovebox for making the active layers. After the formation of the perovskite layer, a solution of PCBM (in chlorobenzene) and BCP (in IPA) were spin-coated at 3000 rpm for 50 s and 6000 rpm for 30 s, respectively. Finally, Ag electrodes of 1000 nm were thermally deposited at a rate of 1 \AA s^{-1} , respectively. The active area as defined by the shadow mask is $\approx 0.04 \text{ cm}^2$. The sample was mounted inside a nitrogen-filled sample holder with a quartz optical window for subsequent measurements. The device's reproducibility is improved by strictly maintaining the moisture/oxygen ratio and temperature in the inert atmosphere glovebox. The light J - V curves were measured on a Keithley 2400 source meter unit under AM 1.5G light illumination with a Newport-Oriel (Sol3A Class AAA Solar Simulator, 94043A) solar simulator operating at an intensity of 100 mW cm^{-2} . The light intensity was calibrated by a certified Oriel reference cell (91150V) and verified with a NREL calibrated, filtered Si diode (Hamamatsu, S1787-04). The J - V profiles were obtained under both forward ($-0.5 \text{ V} \rightarrow +1.5 \text{ V}$) and reverse ($+1.5 \text{ V} \rightarrow -0.5 \text{ V}$) scans. External quantum efficiency (EQE) spectra were measured on a commercial EQE set-up (QE-R, Enli Technology Co., Ltd). A calibrated silicon diode with a known spectral response was used as a reference.

Supporting Information

Supporting Information is available from the Wiley Online Library or from the author.

Acknowledgements

This work was supported by National Natural Science Foundation of China (NSFC)—The Swedish Foundation for International Cooperation in Research and Higher Education (STINT) under grant No. 5191101797 and International Cooperation Project of Ministry of Science and Technology (MOST) under grant No. 2017YFE0107800 (Z.L.). K.Z. acknowledges the support by Danish Council for Independent Research No. 7026-0037B and Swedish Research Council No. 2017-05337. The work performed in Lund is supported by Swedish Energy Agency Grant No. 446511-1, Swedish research council, STINT, Crafood, and KAW foundation. The authors gratefully express thanks for the beam time and technical supports provided by the BL14B1 GIWAXS beamline at Shanghai Synchrotron Radiation facility (SSRF).

Conflict of Interest

The authors declare no conflict of interest.

Data Availability Statement

Research data are not shared.

Keywords

2D perovskites, asymmetric aromatic spacers, Dion-Jacobson, out-of-plane carrier transport, staggered alignment

Received: May 7, 2021

Revised: July 28, 2021

Published online: August 12, 2021

- [1] L. Mao, C. C. Stoumpos, M. G. Kanatzidis, *J. Am. Chem. Soc.* **2019**, *141*, 1171.
- [2] X. Li, W. Ke, B. Traoré, P. Guo, I. Hadar, M. Kepenekian, J. Even, C. Katan, C. C. Stoumpos, R. D. Schaller, M. G. Kanatzidis, *J. Am. Chem. Soc.* **2019**, *141*, 12880.
- [3] F. Li, J. Zhang, S. Jo, M. Qin, Z. Li, T. Liu, X. Lu, Z. Zhu, A. K. Y. Jen, *Small Methods* **2019**, *4*, 1900831.
- [4] D. Ghosh, D. Acharya, L. Pedesseau, C. Katan, J. Even, S. Tretiak, A. J. Neukirch, *J. Mater. Chem. A* **2020**, *8*, 22009.
- [5] E. R. Dohner, A. Jaffe, L. R. Bradshaw, H. I. Karunadasa, *J. Am. Chem. Soc.* **2014**, *136*, 13154.
- [6] J. Lu, L. Jiang, W. Li, F. Li, N. K. Pai, A. D. Scully, C.-M. Tsai, U. Bach, A. N. Simonov, Y.-B. Cheng, L. Spiccia, *Adv. Energy Mater.* **2017**, *7*, 1700444.
- [7] I. Spanopoulos, W. Ke, C. C. Stoumpos, E. C. Schueller, O. Y. Kontsevoi, R. Seshadri, M. G. Kanatzidis, *J. Am. Chem. Soc.* **2018**, *140*, 5728.
- [8] S. Ahmad, P. Fu, S. Yu, Q. Yang, X. Liu, X. Wang, X. Wang, X. Guo, C. Li, *Joule* **2019**, *3*, 794.
- [9] C. Ma, D. Shen, T.-W. Ng, M.-F. Lo, C.-S. Lee, *Adv. Mater.* **2018**, *30*, 1800710.
- [10] P. Li, C. Liang, X. L. Liu, F. Li, Y. Zhang, X. T. Liu, H. Gu, X. Hu, G. Xing, X. Tao, Y. Song, *Adv. Mater.* **2019**, *31*, 1901966.
- [11] L. Mao, S. M. L. Teicher, C. C. Stoumpos, R. M. Kennard, R. A. DeCrescent, G. Wu, J. A. Schuller, M. L. Chabinyk, A. K. Cheetham, R. Seshadri, *J. Am. Chem. Soc.* **2019**, *141*, 19099.
- [12] Y. Lv, H. Ma, Y. Yin, Q. Dong, W. Zhao, S. Jin, Y. Shi, *J. Mater. Chem. A* **2020**, *8*, 10283.

- [13] X. Jiang, J. Zhang, S. Ahmad, D. Tu, X. Liu, G. Jia, X. Guo, C. Li, *Nano Energy* **2020**, *75*, 104892.
- [14] L. Mao, Y. Wu, C. C. Stoumpos, M. R. Wasielewski, M. G. Kanatzidis, *J. Am. Chem. Soc.* **2017**, *139*, 5210.
- [15] W. Ke, L. Mao, C. C. Stoumpos, J. Hoffman, I. Spanopoulos, A. D. Mohite, M. G. Kanatzidis, *Adv. Energy Mater.* **2019**, *9*, 1803384.
- [16] L. Mao, W. Ke, L. Pedesseau, Y. Wu, C. Katan, J. Even, M. R. Wasielewski, C. C. Stoumpos, M. G. Kanatzidis, *J. Am. Chem. Soc.* **2018**, *140*, 3775.
- [17] E. S. Vasileiadou, B. Wang, I. Spanopoulos, I. Hadar, A. Navrotsky, M. G. Kanatzidis, *J. Am. Chem. Soc.* **2021**, *143*, 2523.
- [18] L. Mao, P. Guo, M. Kepenekian, I. Spanopoulos, Y. He, C. Katan, J. Even, R. D. Schaller, R. Seshadri, C. C. Stoumpos, M. G. Kanatzidis, *J. Am. Chem. Soc.* **2020**, *142*, 8342.
- [19] M. J. u M. Chen, M. Hu, Z. Dai, Y. Hu, Y. Rong, H. Han, X. Zeng, Y. Zhou, N. P. Padture, *ACS Energy Lett.* **2019**, *4*, 276.
- [20] I.-H. Park, K. C. Kwon, Z. Zhu, X. Wu, R. Li, Q.-H. Xu, K. P. Loh, *J. Am. Chem. Soc.* **2020**, *142*, 18592.
- [21] I.-H. Park, Q. Zhang, K. C. Kwon, Z. Zhu, W. Yu, K. Leng, D. Giovanni, H. S. Choi, I. Abdelwahab, Q.-H. Xu, T. C. Sum, K. P. Loh, *J. Am. Chem. Soc.* **2019**, *141*, 15972.
- [22] L. Mao, R. M. Kennard, B. Traore, W. Ke, C. Katan, J. Even, M. L. Chabinyc, C. C. Stoumpos, M. G. Kanatzidis, *Chem* **2019**, *5*, 2593.
- [23] H. Wang, Z. Qin, J. Xie, S. Zhao, K. Liu, X. Guo, G. Li, X. Lu, K. Yan, J. Xu, *Small* **2020**, *16*, 2003098.
- [24] T. Ishihara, J. Takahashi, T. Goto, *Phys. Rev. B: Condens. Matter Mater. Phys.* **1990**, *42*, 11099.
- [25] J. M. Hoffman, J. Strzalka, N. C. Flanders, I. Hadar, S. A. Cuthriell, Q. Zhang, R. D. Schaller, W. R. Dichtel, L. X. Chen, M. G. Kanatzidis, *Adv. Mater.* **2020**, *32*, 2002812.
- [26] Y. Miao, Y. Chen, H. Chen, X. Wang, Y. Zhao, *Chem. Sci.* **2021**, *12*, 7231.
- [27] J. Kim, T. Hwang, B. Lee, S. Lee, K. Park, H. H. Park, B. Park, *Small Methods* **2019**, *3*, 1800361.
- [28] J. Wang, D. Lin, Y. Chen, S. Luo, L. Ke, X. Ren, S. Cui, L. Zhang, Z. Li, K. Meng, Y. Lin, L. Ding, Y. Yuan, *Sol. RRL* **2020**, *4*, 2000371.
- [29] D. Lu, G. Lv, Z. Xu, Y. Dong, X. Ji, Y. Liu, *J. Am. Chem. Soc.* **2020**, *142*, 11114.
- [30] Y. Li, J. V. Milić, A. Ummadisingu, J.-Y. Seo, J.-H. Im, H.-S. Kim, Y. Liu, M. I. Dar, S. M. Zakeeruddin, P. Wang, A. Hagfeldt, M. Grätzel, *Nano Lett.* **2018**, *19*, 150.
- [31] B.-E. Cohen, Y. Li, Q. Meng, L. Etgar, *Nano Lett.* **2019**, *19*, 2588.
- [32] Y. Shang, Y. Liao, Q. Wei, Z. Wang, B. Xiang, Y. Ke, W. Liu, Z. Ning, *Sci. Adv.* **2019**, *5*, eaaw8072.
- [33] S. Yuan, Z. K. Wang, L. X. Xiao, C. F. Zhang, S. Y. Yang, B. B. Chen, H. T. Ge, Q. S. Tian, Y. Jin, L. S. Liao, *Adv. Mater.* **2019**, *31*, 1904319.
- [34] M. C. Gélvez-Rueda, P. Ahlawat, L. Merten, F. Jahanbakhshi, M. Mladenović, A. Hinderhofer, M. I. Dar, Y. Li, A. Dučinskas, B. Carlsen, W. Tress, A. Ummadisingu, S. M. Zakeeruddin, F. Schreiber, A. Hagfeldt, U. Rothlisberger, F. C. Grozema, J. V. Milić, M. Graetzel, *Adv. Funct. Mater.* **2020**, *30*, 2003428.
- [35] A. Dučinskas, G. Y. Kim, D. Moia, A. Senocrate, Y.-R. Wang, M. A. Hope, A. Mishra, D. J. Kubicki, M. Siczek, W. Bury, T. Schneeberger, L. Emsley, J. V. Milić, J. Maier, M. Grätzel, *ACS Energy Lett.* **2021**, *6*, 337.
- [36] S. Yu, Y. Yan, M. Abdellah, T. Pullerits, K. Zheng, Z. Liang, *Small* **2019**, *15*, 1905081.
- [37] R. Quintero-Bermudez, A. H. Proppe, A. Mahata, P. Todorovic, E. H. Sargent, *J. Am. Chem. Soc.* **2019**, *141*, 13459.
- [38] Y. Qin, H. Zhong, J. J. Intemann, S. Leng, M. Cui, C. Qin, M. Xiong, F. Liu, A. K. Y. Jen, K. Yao, *Adv. Energy Mater.* **2020**, *10*, 1904050.
- [39] J. Qing, X. Liu, M. Li, F. Liu, Z. Yuan, E. Tiukalova, Z. Yan, M. Duchamp, S. Chen, Y. Wang, S. Bai, J. M. Liu, H. J. Snaith, C. S. Lee, T. C. Sum, F. Gao, *Adv. Energy Mater.* **2018**, *8*, 1800185.
- [40] K. Zheng, Y. Chen, Y. Sun, J. Chen, P. Chábera, R. Schaller, M. J. Al-Marri, S. E. Canton, Z. Liang, T. Pullerits, *J. Mater. Chem. A* **2018**, *6*, 6244.
- [41] V. D'Innocenzo, G. Grancini, M. J. P. Alcocer, A. R. S. Kandada, S. D. Stranks, M. M. Lee, G. Lanzani, H. J. Snaith, A. Petrozza, *Nat. Commun.* **2014**, *5*, 3586.
- [42] H. Yu, Y. Xie, J. Zhang, J. Duan, X. Chen, Y. Liang, K. Wang, L. Xu, *Adv. Sci.* **2021**, 2004510.